PAPER

Check for updates

Enhanced triboelectric properties of Eu₂O₃-doped BaTiO₃/PVDF-HFP nanofibers†

Xin-Xian Wu,[a,b] Jun-Jie Zhang,[a] Chia-Hsien Lee[a,c] and Meng-Fang Lin ⓘ *[a,b,c]

Because triboelectric nanogenerators (TENGs) convert mechanical energy into electricity, they are sustainable energy sources for powering a diverse range of intelligent sensing and monitoring devices. To enhance the electrical output of polymer-based TENGs, nanofillers are commonly incorporated into polymers. In this study, we developed a simple low-temperature process for preparing high-performance ceramic powder-based TENGs comprising electrospun fibrous surfaces based on poly(vinylidene difluoride-*co*-hexafluoropropylene) (PVDF-HFP) and dispersed Eu_2O_3-doped $BaTiO_3$ nanofillers. Herein, we discuss the effect of the modified dielectric properties and transferred charge of the electrification film on the performance of the TENGs. After incorporating the Eu_2O_3-doped $BaTiO_3$ nanofiller, the maximum output voltage of the 10 wt% Eu_2O_3–$BaTiO_3$/PVDF-HFP electrospun-nanofiber TENG reached as high as 1004 V with a corresponding current density of 9.9 μA cm^{-2}. The enhancement in the triboelectric properties of the Eu_2O_3–$BaTiO_3$/PVDF-HFP electrospun-nanofiber TENGs was due to their high amounts of interface polarization and transferred charge, suggesting improved capture and storage of triboelectric electrons. These Eu_2O_3–$BaTiO_3$/PVDF-HFP electrospun-nanofiber TENGs could harvest mechanical energy and power electronic devices; they were robust and not affected by the operating temperature or humidity. Furthermore, we used a fabricated device as a sensor for application as a light-emitting diode dimmer switch and for the tracking of leg movement.

Introduction

Energy harvesting technologies can be classified simply, according to their energy sources, as photovoltaic cells, thermoelectric devices, and piezo/triboelectric nanogenerators.[1] Triboelectric nanogenerators (TENGs) are devices that convert mechanical energy into electricity through electrification and electrostatic effects.[2–4] Some TENGs generate a high-voltage output energy based on waste energy sources and are not restricted by space, weather, or time.[1] Furthermore, TENGs are attractive due to their low fabrication cost, light weight, and high energy efficiency, as well as a wide range of materials and structures available to choose from in the design stage,[5,6] leading to a large variety of viable device setups.[7–10] Many investigations have focused on the effects of the material selection,[11–13] surface modification,[14–17] and surface morphology[18–21] of the triboelectric materials on the performance of the resulting TENGs. For example, the surface morphology of the friction layers plays a significant role in enhancing the surface charge density of a triboelectric material, thereby affecting the material's specific ability to donate or accept electrons, while the effective surface area affects the output performance of a TENG.[22] Several methods are available to introduce micro/nanostructures into electro-frictional layers—including soft lithography,[21,23,24] photolithography,[18] and ultrafast laser patterning[25,26]—to increase the surface charge density and, in turn, the output performance of the triboelectric harvester. Wang *et al.* reported the rational design of an arch-shaped structure based on contact electrification between a polymer and a metal film.[21] Such technologies can, however, be costly, time-consuming, and limited in terms of the area of treatment, or require multi-step manufacturing techniques to achieve the required surface appearance, making it challenging to use them in production processes on the industrial scale. Recently, progress has been made in fabricating nanofiber-based TENGs for unobtrusive biomechanical energy harvesting, as well as continuous, real-time, and noninvasive health monitoring.[27,28] Electrospun membranes possessing high breathability, great flexibility, and controllable thickness, combined with ease of manufacturing, have great potential for use in wearable devices.[29–31] Furthermore, electro-

[a]Department of Materials Engineering, Ming Chi University of Technology, New Taipei City, Taiwan
[b]Center for Plasma and Thin Film Technologies, Ming Chi University of Technology, New Taipei City, Taiwan
[c]Research Center for Intelligent Medical Devices, Ming Chi University of Technology, New Taipei City, Taiwan
†Electronic supplementary information (ESI) available. See DOI: https://doi.org/10.1039/d2nr05990h

spinning is capable of producing membranes with micro/nano architectures and high surface roughness, potentially improving the contact area and friction effect to enhance the output performance of triboelectric materials.[32–35] Through electrospinning, polymers can be fabricated conveniently into nanofiber membranes having high surface roughness, large specific surface areas, and good flexibility, making them well suited for development into TENGs.[3,36]

The fundamental working principle of a TENG involves a combination of contact electrification and electrostatic induction. Contact electrification provides static polarized charges; electrostatic induction is the main mechanism that converts mechanical energy to electricity. Because the most common setup of a TENG is essentially a plate-capacitor with a varying gap thickness, TENGs exhibit similar capacitive behavior, including an increasing amount of stored charge improving their performance. Therefore, the performance of a TENG is affected by the dielectric constant of the friction layer. The pristine polymers used for TENGs usually provide relatively low triboelectric outputs that are insufficient for practical application.[37,38] Incorporating a nanofiller having a high dielectric constant (*e.g.*, ZnO,[39] TiO_2,[2] $SrTiO_3$,[40] $ZnSnO_3$,[41] $BaTiO_3$,[42–45] and $CaCu_3TiO_4O_{12}$[46]) into the polymer can lead to an enhancement in properties by providing electron trapping sites or increasing the relative permittivity of the nanocomposite.[47] Among such nanofillers, $BaTiO_3$ has attracted much attention because its permittivity is higher than those of ZnO[39] and TiO_2,[2] and because it is more convenient to prepare at a lower cost relative to $CaCu_3Ti_4O_{12}$.[46] Kang *et al.* improved the performance of TENGs by adding $BaTiO_3$ nanoparticles to poly(vinylidene difluoride) (PVDF) to improve its dielectric constant.[42] Tao *et al.* reported an enhanced TENG performance when using a $BaTiO_3$/PVDF film as the negative tribomaterial and a polyamide-6 (PA6) film as the positive tribomaterial.[43] Nevertheless, the friction layers of those $BaTiO_3$/PVDF nanocomposite films, prepared using blade-casting or spin-

coating, lacked the surface roughness needed to enhance the contact area between the friction layers and, thereby, the triboelectric performance. In addition, an extremely high force (>180 N) has to be applied to the TENG, an unrealistic requirement for applications useful in daily life.[43]

In conventional processing, high-temperature sintering is required for the doping of rare-earth oxides in $BaTiO_3$ bulk ceramics to obtain high dielectric constants. In the present study, we synthesized europium oxide (Eu_2O_3)-doped $BaTiO_3$ hollow nanoparticles of high dielectric constant through a simple hydrothermal method, without the assistance of a surfactant or high-temperature sintering.[48] Because soft nanofibers having high specific surface areas are excellent choices for wearable TENGs, we incorporated a hollow Eu_2O_3-doped $BaTiO_3$ nanofiller into poly(vinylidene difluoride-*co*-hexafluoropropylene) (PVDF-HFP) to produce nanofiber mats, significantly improving the electrical output of PVDF copolymer-based TENGs. The maximum output voltage of our 10 wt% Eu_2O_3–$BaTiO_3$/PVDF-HFP electrospun-nanofiber TENG reached as high as 1004 V with a current density of 9.9 μA cm^{-2}. Notably, the electrical output of our TENG fabricated from Eu_2O_3–$BaTiO_3$/PVDF-HFP nanofiber mats was very competitive with those of previously reported ceramic powder-based TENGs. Furthermore, our fabricated TENG remained stable when tested at various temperatures and humidity points and for over 20 000 cycles. In addition, we could use our developed electrospun nanofiber TENG to power a 1000-light emitting diode (LED) bulb array and a digital watch. Moreover, this electrospun-nanofiber TENG device could be used not only as a self-powering device, but also as a sensor; here, we used it as an LED light dimmer switch and to track leg movement, demonstrating its practicality for sensor applications.

Experimental

Eu_2O_3-doped $BaTiO_3$ nanopowder

Eu_2O_3 solutions were prepared by varying the ratio of Eu_2O_3 and glacial acetic acid at 25 °C and then slowly adding de-ionized water (2 mL). Ultrasonication for 30 min led to the Eu_2O_3 solution becoming transparent, indicating the good dissolution of Eu_2O_3. Subsequently, titanium(IV) isopropoxide was added slowly into the Eu_2O_3 solution with moderate agitation overnight. The initially hazy solution turned clear upon the hydrolysis of titanium isopropoxide to give a titanium acylated solution. A mixed solution was prepared by adding dissolved barium acetate solution into Eu_2O_3/titanium acylated solution. For the optimization of the stoichiometric ratio of the synthesized powder, the molar ratio of barium acetate to titanium acylate in the solution was fixed at 1.8 : 1. To prepare fine powders, mixed solutions of the Ba and Eu_2O_3–titanium acylated precursors were added into a NaOH solution with vigorous agitation. The precipitated solutions underwent a hydrothermal reaction in an autoclave. Based on the particle morphology and crystallinity, performing the hydrothermal reaction at 220 °C for 2 h appeared to be optimal for hollow nano-

Dr Meng-Fang Lin received her Ph. D. degree from the School of Materials Science and Engineering, Nanyang Technological University (NTU), Singapore, in 2013. She joined the Department of Materials Engineering as an Assistant Professor in 2020. She did post-doctoral research at National Institute for Materials Science (NIMS), Japan (2013–2014). She was a senior research fellow at NTU (2015–2018). Her research focuses on triboelectric energy harvesting, nanomaterials for energy and electronics applications, pressure sensors, and the human–machine interface.

Meng-Fang Lin

particle formation. When the reaction was completed, the product solution was centrifuged (8000 rpm) and washed three times with deionized water. The washed powders were dried for 12 h at 100 °C on a hot plate.[48]

Eu_2O_3–$BaTiO_3$/PVDF-HFP nanofiber mats

The hollow Eu_2O_3-doped $BaTiO_3$ nanopowder was sonicated after adding acetone to prevent agglomeration. PVDF-HFP (17 wt%) was dissolved in tetrahydrofuran (THF) at 60 °C for 2 h. When the solution became transparent, the solution of the hollow Eu_2O_3-doped $BaTiO_3$ was added into the PVDF-HFP solution. Composite solutions of Eu_2O_3–$BaTiO_3$/PVDF-HFP were prepared through continuous stirring of mixtures of Eu_2O_3–$BaTiO_3$ overnight at various weight percentages with PVDF-HFP/THF. Electrospinning was used to fabricate Eu_2O_3–$BaTiO_3$/PVDF-HFP nanofibers. A composite solution of Eu_2O_3–$BaTiO_3$/PVDF-HFP was electrospun—using a 19 G blunt needle, at a voltage of 18 kV, a pump rate of 3 mL h^{-1}, and a needle-to-collector distance of 130 mm—to form the nanofibers. All nanofibers were collected over aluminum foil, which was used as a ground surface.

Material characterization

Detailed views of the hollow structures were obtained using transmission electron microscopy (TEM, JEOL JEM-2100 LaB_6), operated at 200 kV. The crystallinity of the as-synthesized nanopowder was identified using X-ray diffraction (XRD, PANalytical Empyrean) and Cu Kα radiation (λ = 1.5418) at 45 kV and 30 mA, with a scan rate of 2° min^{-1} from 10 to 80° (2θ). Field emission scanning electron microscopy (FE-SEM, JEOL JSM-6701F), operated at 5 kV, was employed to determine the particle morphology and size. Scanning electron microscopy (SEM, JEOL JSM-6390) was performed at 8 kV to determine the morphologies of the nanofibers and the deposited Pt layer. Raman spectra were recorded using a Horiba HR 550 spectrometer, at an excitation wavelength of 532 nm. Dielectric constants were measured using an M6632 apparatus. The transferred charge was measured using a Keithley 6517B system electrometer. The surface potentials of the fabricated nanofiber mats were measured using an electrostatic voltmeter (Dong Il Technology, Model ARM-S050). The voltage and current output from the triboelectric device were measured using an oscilloscope (Tektronix, Model DPO 3040). The dynamic mechanical pressure was applied by using a magnetic shaker (Sinocera, Model JZK-20) under various forces (1–40 N) and at various frequencies (1–10 Hz). The surface charge was measured using a Keithley 6517B system electrometer (impedance: >200 TΩ). An Arduino UNO R3 Atmega 328p was used to prepare the LED dimmer switch.

Results and discussion

We synthesized the single-crystalline Eu_2O_3-doped hollow $BaTiO_3$ nanoparticles through a simple hydrothermal method involving a Kirkendall effect–induced hollowing mechanism,[48]
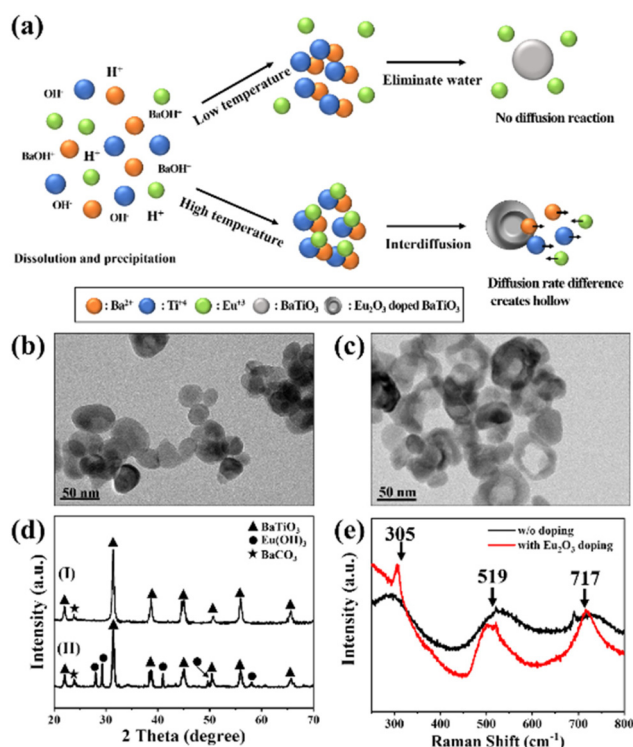

Fig. 1 (a) Schematic representation of the mechanism of formation of hollow nanoparticles through the Kirkendall effect. (b and c) TEM images of the $BaTiO_3$ nanoparticles prepared (b) without and (c) with Eu_2O_3 doping. (d) XRD patterns of the $BaTiO_3$ nanoparticles prepared (I) without and (II) with Eu_2O_3 doping. (e) Raman spectra of the $BaTiO_3$ nanoparticles prepared with and without Eu_2O_3 doping.

as displayed in Fig. 1(a). In the initial stage, dissolution and precipitation occurred, with aqueous Ba^{2+} species reacting with hydrolyzed Ti species by eliminating a water molecule to form $BaTiO_3$ nanoparticles at a low temperature[49] [Fig. 1(b)]. It has been reported that the $BaTiO_3$ powders prepared through the hydrothermal method contain a large number of protons in the oxygen sublattice, with the proton defects being compensated for by the simultaneous formation of barium and titanium vacancies.[50,51] During the high-temperature reaction, the $Eu(OH)_3$ molecules dissociate and fill the Ba and Ti vacancies through interdiffusion, while water molecules condense and move outward. The outward diffusion rate of water is higher than the inward diffusion of $Eu(OH)_3$, resulting in hollow $BaTiO_3$ nanoparticles [Fig. 1(c)]. Fig. S1† displays our process for the optimization of the synthesized hollow $BaTiO_3$ nanoparticles. The synthesis temperature played an important role in the morphological evolution of the $BaTiO_3$ nanostructures. The optimal conditions for the synthesis involved doping with 20 at% Eu_2O_3 at 220 °C for 2 h. We used XRD to examine the crystallinity of the $BaTiO_3$ nanoparticles prepared with and without Eu_2O_3 [Fig. 1(d)]. When the Eu^{3+} ions were introduced, they could access the lattice of $BaTiO_3$, due to their similar ionic radius and charge. The XRD peaks of the Eu_2O_3-doped $BaTiO_3$ nanoparticles matched those of tetra-

gonal $BaTiO_3$ (JCPDS card 75-0583: a = 3.995 Å; c = 4.034 Å). After doping with Eu_2O_3, the excess Eu^{3+} ions existed in the form of an $Eu(OH)_3$ phase (JCPDS card 17-0781: a = 6.365 Å; c = 3.645 Å). Fig. 1(e) displays the Raman spectra of the $BaTiO_3$ nanoparticles prepared with and without Eu_2O_3 doping. We assign the peaks near 519 cm^{-1} to the fundamental transverse component of the optical (TO) mode of A1 symmetry, and the band near 717 cm^{-1} to eventual Ba^{2+}. Furthermore, the peak at 717 cm^{-1} represents the presence of OH lattice groups, which can reside as defects on oxygen sites within $BaTiO_3$.[52] Compared with the spectrum of the $BaTiO_3$ nanoparticles prepared without doping Eu_2O_3, the spectrum of Eu_2O_3-doped $BaTiO_3$ showed an extra peak at 305 cm^{-1}, representing tetragonal $BaTiO_3$ because of its narrow width and the invariance of its peak position as a function of crystal orientation.[53] This signal suggested the existence of tetragonal distortions in the hollow doped $BaTiO_3$ nanoparticles.

Next, we investigated the morphology of the nanofibers, because it would significantly affect the surface roughness and, thereby, the TENG performance. Electrospinning is a versatile and promising technique for fabricating polymeric nanofiber mats for energy harvesting and intelligent sensing. In particular, electrospun nanofiber mats possess high surface roughness and, therefore, can increase the effective contact area and accumulated surface charge density when employed in TENGs, enhancing their triboelectric performance. Fig. 2(a) shows an SEM image of the pristine electrospun PVDF-HFP, revealing completely nanofiber structures with diameters ranging from approximately 300 to 900 nm. Fig. 2(b) and (c) reveal the Eu_2O_3–$BaTiO_3$/PVDF-HFP nanofiber morphology. Fig. S2† shows the Eu_2O_3–$BaTiO_3$/PVDF-HFP nanofiber mor-

phologies obtained at the various weight percentages. The average nanofiber diameter of 0, 1, 5, 10, and 15 weight percentages of the Eu_2O_3–$BaTiO_3$/PVDF-HFP nanofiber was 0.51, 0.59, 0.52, 0.53, and 0.58 μm, respectively. The average nanofiber diameter is increased upon increasing the weight percentage of Eu_2O_3–$BaTiO_3$/PVDF-HFP due to nanoparticle agglomeration issues. The average nanofiber diameter distribution is from 0.3 μm to 1 μm. The thickness of the 10 wt% Eu_2O_3–$BaTiO_3$/PVDF-HFP nanofiber is around 376 μm.

Compared with the pristine electrospun PVDF-HFP nanofibers, the Eu_2O_3–$BaTiO_3$/PVDF-HFP nanofibers featured connected beads, with some of the nanofibers wrapping the surfaces of the beads, which incorporated Eu_2O_3–$BaTiO_3$ nanoparticles.

It has been reported that such extra beads can enhance the electrical performance by providing a higher surface roughness.[54] Fig. 2(d) and (e) show the XRD patterns and Fourier transform infrared (FTIR) spectra, respectively, of the Eu_2O_3–$BaTiO_3$/PVDF-HFP nanofibers prepared at various weight percentages. The XRD patterns of the pristine PVDF-HFP nanofiber mats could be indexed according to the α, β, and γ PVDF crystal phases. The peak at 17.9° corresponds to the PVDF α-phase; the broad peak at 19.2° corresponds to the superposition of the β-phase diffraction.[55] The characteristic diffraction peaks of $BaTiO_3$ were the same as those in Fig. 1(d). Upon increasing the amount of the Eu_2O_3-doped $BaTiO_3$ nanofiller, the characteristic diffraction peaks of $BaTiO_3$ increase in intensity relative to those of pristine PVDF-HFP. It should be noted that increasing the weight percentage of the nanofiller will affect the ratio between the alpha and beta phase of PVDF-HFP in favor of the beta phase as shown in Fig. S3.† However, since the change in the electronic properties mainly originates from the nanofiller, it does not influence the presented results. The FTIR spectra of all of the nanofibers showed signals at 1401 cm^{-1} for CH_2 wagging and near 875 cm^{-1} for C–C skeleton vibrations. The bands near 1068 cm^{-1} (C–F stretching) and 1180 cm^{-1} (CF_3 stretching) were characteristic of HFP units.[56] The bands near 841 and 1277 cm^{-1} indicated that the PVDF-HFP in the electrospun nanofibers was present primarily in the β-phase.

We examined the electrical properties of the nanofiber films. Fig. 3(a) displays the dependence of the dielectric constant of the various weight percentages of the Eu_2O_3–$BaTiO_3$/PVDF-HFP nanofiber mats on the frequency of the applied electric field. The polarizability of a dielectric material changes with the frequency of the applied electric field, contributing to the variation of the capacitance and the relative dielectric permittivity. At lower frequencies, the orientation of the dipoles of the Eu_2O_3–$BaTiO_3$/PVDF-HFP nanofibers was not affected significantly, thereby leading to higher dielectric constants. At higher frequencies, the dipoles could not maintain their orientation in the presence of the alternating field, resulting in lower relative dielectric permittivities. According to the relationship between the transferred charge and the dynamic capacitance of a TENG, increasing the interface polarization will also lead to an enhanced performance of the
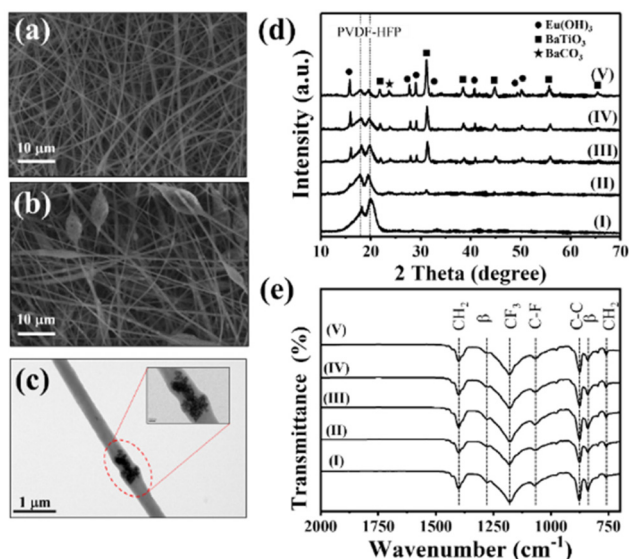

Fig. 2 (a and b) SEM images of electrospun (a) pristine PVDF-HFP nanofibers and (b) 10 wt% Eu_2O_3–$BaTiO_3$/PVDF-HFP nanofibers. (c) TEM image of an electrospun Eu_2O_3–$BaTiO_3$/PVDF-HFP nanofiber. (d) XRD patterns and (e) FTIR spectra of the (I) 0, (II) 1, (III) 5, (IV) 10, and (V) 15 wt% Eu_2O_3–$BaTiO_3$/PVDF-HFP nanofibers.
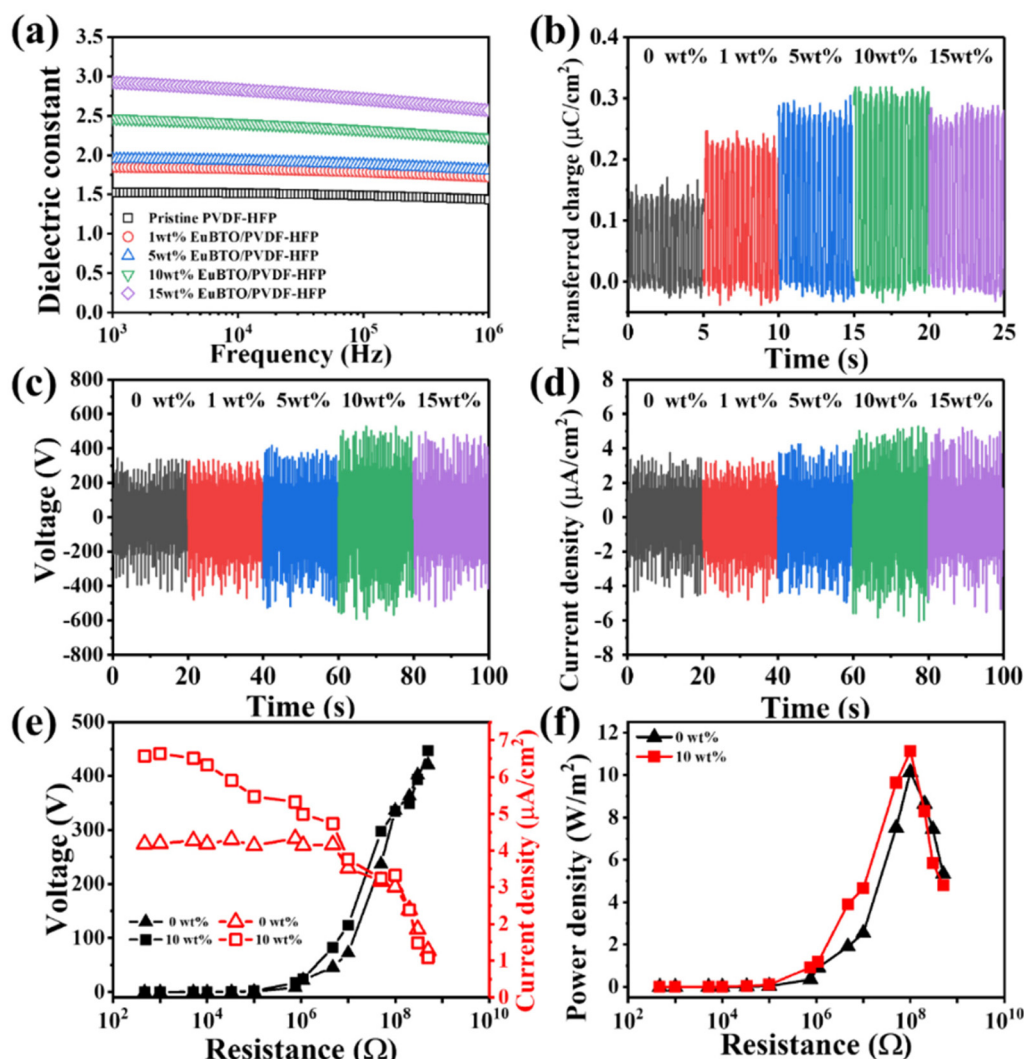
Fig. 3 (a) Frequency-dependence of the dielectric constant of various-weight-percentage $Eu_2O_3-BaTiO_3$/PVDF-HFP nanofiber mats. (b) Transferred charge of various-weight-percentage $Eu_2O_3-BaTiO_3$/PVDF-HFP nanofiber mats after contact friction with the Kapton film. (c) Maximum output voltage and (d) current density of the TENGs composed of various-weight-percentage $Eu_2O_3-BaTiO_3$/PVDF-HFP nanofibers, measured at 40 N and 5 Hz. (e) Output voltage and current density and (f) power density of TENGs composed of various-weight-percentage $Eu_2O_3-BaTiO_3$/PVDF-HFP nanofibers, plotted with respect to resistance.

TENG. The increase in the dielectric constant of the Eu_2O_3- $BaTiO_3$/PVDF-HFP nanofibers compared with that of pristine PVDF-HFP as the amount of filler content is increased can be attributed to interfacial polarization (*i.e.*, a Maxwell–Wagner–Sillars effect) indicating the improvement of the electrical output of the TENG.[48,57] The dielectric constants of all of the electrospun nanofibers were relatively low because their highly porous structures were filled with air, which showed a low dielectric constant. Fig. S4(a)† reveals that the dielectric loss of the various-weight-percentage $Eu_2O_3-BaTiO_3$/PVDF-HFP nanofibers increased upon increasing the volume-fraction of $Eu_2O_3-BaTiO_3$, suggesting a poorer ability to capture and store triboelectric electrons. Fig. S4(b)† shows the initial surface potentials of the different weight percentages of the Eu_2O_3-doped $BaTiO_3$/PVDF-HFP composite. Compared with pristine

PVDF-HFP, the initial surface potentials of the Eu_2O_3-doped $BaTiO_3$/PVDF-HFP composite were higher, indicating that the surface charge increased after adding the Eu_2O_3-doped $BaTiO_3$ nanoparticle, resulting in an enhanced electrical output. The Eu_2O_3-doped $BaTiO_3$ nanofillers played an important role in enhancing the frictional surface potential. Fig. 3(b) reveals that the transferred charges of the $Eu_2O_3-BaTiO_3$/PVDF-HFP nanofibers of various weight percentages increased upon increasing the content of the hollow $Eu_2O_3-BaTiO_3$ nanoparticles up to 10 wt%. The transferred charge decreased slightly at 15 wt% nanofiller, due to higher dielectric loss when compared with that at 10 wt% nanofiller. Hence, the 10 wt% $Eu_2O_3-BaTiO_3$/PVDF-HFP nanofibers possessed the highest amount of transferred charge, due to a higher dielectric constant and lower dielectric loss. The higher amount of

the transferred charge was a consequence of the improved capture and storage of triboelectric electrons, thereby promoting the corresponding output. We used the electrospun nanofibers to fabricate TENGs for mechanical energy harvesting (Fig. S5†). We measured the electrical output of the various-weight-percentage Eu_2O_3–$BaTiO_3$/PVDF-HFP electrospun nanofibers while varying the operating frequency and applied external force (Fig. S6–S9†). Increasing the compressive force led to significantly improved contact between the triboelectric layers, thereby resulting in the generation of more electric charges. Increasing the operating frequency resulted in more intense friction, which generated more charges, due to the greater rate of contact between the Eu_2O_3–$BaTiO_3$/PVDF-HFP electrospun nanofibers and the Kapton layer. The measured electrical outputs of the Eu_2O_3–$BaTiO_3$/PVDF-HFP electrospun-nanofiber TENG were higher when operated at 5 Hz, but the generation of electricity was not very stable. This instability is because, at these high frequencies, the contact and separation processes of the triboelectric layers were incomplete, preventing the surface charge from reaching its maximum value. Therefore, we chose a cyclic compressive force of 40 N applied at a frequency of 3 Hz as the optimal operation conditions for subsequent experiments. Fig. 3(c) and (d) show the electrical output voltages and current densities, respectively, of the various-weight-percentage Eu_2O_3–$BaTiO_3$/PVDF-HFP electrospun-nanofiber TENGs. The peak output voltage and current density both increased upon increasing the weight percentage of the nanofiller up to 10 wt%, due to higher amounts of transferred charge. The maximum output voltage of the 10 wt% Eu_2O_3–$BaTiO_3$/PVDF-HFP electrospun-nanofiber TENG reached as high as 1004 V with a corresponding current density of 9.9 μA cm^{-2}; these values are the highest ever reported for the ceramic powder–based TENGs (Table 1). We evaluated the electrical output performance of our developed TENGs in comparison with other ceramic powder–related TENGs reported previously in the literature, in terms of open-circuit voltage, current density, surface charge density, peak power density, and materials used. Table 1 reveals that the performance of the TENG developed in this study was higher than those of the other ceramic powder–based TENGs. Fig. S10† plots the open-circuit voltage and peak power for our TENG and for those reported previously; our system occupies a very

competitive position. The combination of the open-circuit voltage and short circuit current led to the maximal power of the 10 wt% Eu_2O_3–$BaTiO_3$/PVDF-HFP electrospun-nanofiber TENG reaching as high as 99 W m^{-2}—a value that is 2.3 times higher than that of the pristine PVDF-HFP electrospun-nanofiber TENG. Moreover, Fig. 3(e) and (f) display the electrical properties of our 10 wt% Eu_2O_3–$BaTiO_3$/PVDF-HFP electrospun-nanofiber TENG under various external load resistances (470–1000 MΩ) when operated at 5 Hz and 40 N. The output voltage began increasing upon increasing the load resistance beyond approximately 10 MΩ; in contrast, the output current density decreased upon increasing the resistance. According to the principle of impedance matching, when the resistance of the external load is equal to the internal resistance of the power supply (namely, the internal resistance of the TENG), the output power reaches its maximum value. Our 10 wt% Eu_2O_3–$BaTiO_3$/PVDF-HFP electrospun-nanofiber TENG exhibited a maximum output power density of 12 W m^{-2} at 100 MΩ; this value is 50 times higher than that reported for a system based on $BaTiO_3$ + PVDF/nylon.[42]

Reliability, durability, and stability are extremely important features for the practical application of any TENG. Fig. 4(a) and (b) illustrate the electrical performance of our 10 wt% Eu_2O_3–$BaTiO_3$/PVDF-HFP electrospun-nanofiber TENG operated at various temperatures and humidities, respectively. Gratifyingly, the electrical output of the TENG remained stable at each temperature and humidity point. To examine the mechanical stability of the device, we monitored the electrical output voltage of our 10 wt% Eu_2O_3–$BaTiO_3$/PVDF-HFP electrospun-nanofiber TENG over a duration of 20 000 cycles; Fig. 4(c) reveals its perfect durability. Fig. 4(d) displays that the electrical output of our 10 wt% Eu_2O_3–$BaTiO_3$/PVDF-HFP electrospun-nanofiber TENG remained stable after storing it for 2 weeks.

A 1000-LED bulb array and digital watch could be powered by 10 wt% Eu_2O_3–$BaTiO_3$/PVDF-HFP electrospun-nanofiber TENGs, as displayed in Fig. 5(a)-(I) and (II) and Movie S1.† Fig. 5(a)-(III) shows the voltage curves obtained when charging the capacitors of varying capacitances (0.1, 1, 2.2, 4.7, and 10 μF) with our 10 wt% Eu_2O_3–$BaTiO_3$/PVDF-HFP electrospun-nanofiber TENG, with the 0.1 μF capacitor undergoing instant charging to 17 V within 34 s— which is faster than that when using the pristine PVDF-HFP electrospun-nanofiber TENG

Table 1 Output performance characteristics of the optimized TENG described herein and other recently reported ceramic powder-based TENGs

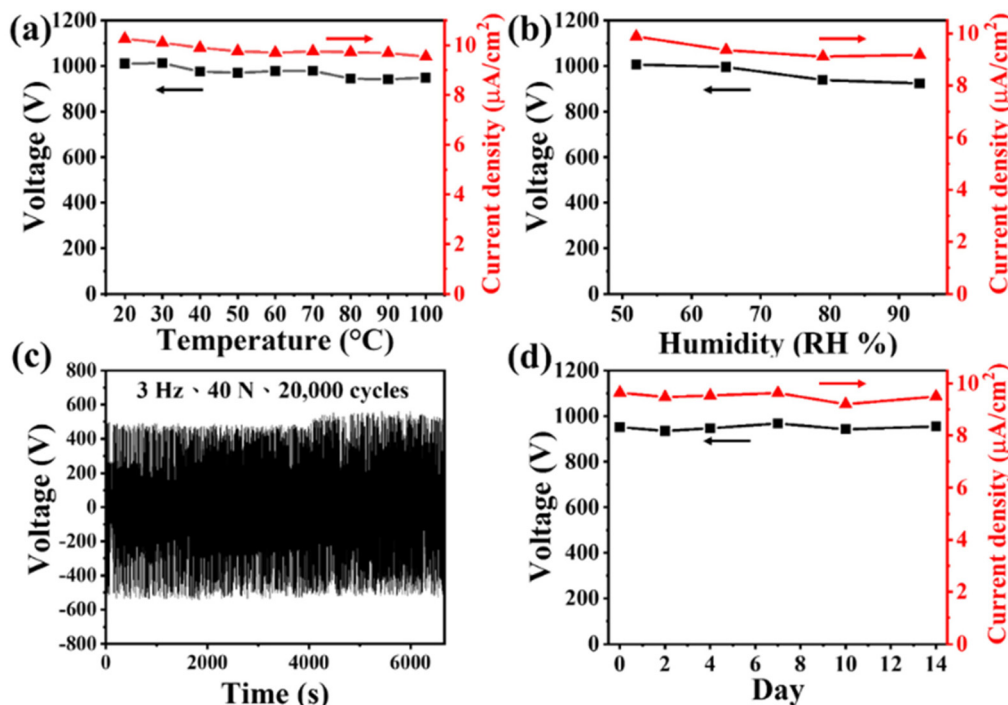| Materials	Voltage (V)	Current density (μA cm^{-2})	Surface charge density (nC cm^{-2})	Power density (W m^{-2})	Ref.
$SrTiO_3$/PDMS	338	9.06	19	6.47	40
$BaTiO_3$/PVDF	161	1.55	12.1	0.225	42
$BaTiO_3$/PVDF	900	1	3.44	9	43
Cubic $BaTiO_3$/PVDF-TrFE	293	5.5	—	2	44
Tetragonal $BaTiO_3$/PVDF-TrFE	315	2.75	—	2.75	44
$BaTiO_3$/PDMS	72.2	0.2	5.3	0.14	45
$CaCu_3Ti_4O_{12}$/PDMS	390	17	10.8	9.6	46
TiO_2/PDMS	125	0.08	1	1	58
$BaTiO_3$/PVDF-HFP	124	1.15	105.6	1.42	59
BNT–BZT/PVDF	400	3.75	—	0.9	60
Eu_2O_3–$BaTiO_3$/PVDF-HFP	**1004**	**9.9**	**330**	**11.12**	**This work**

Fig. 4 Electrical output of the 10 wt% Eu_2O_3–$BaTiO_3$/PVDF-HFP electrospun-nanofiber TENG (a) at various temperatures, (b) at various humidities, (a) during long-term cycling, and (d) during stability testing.
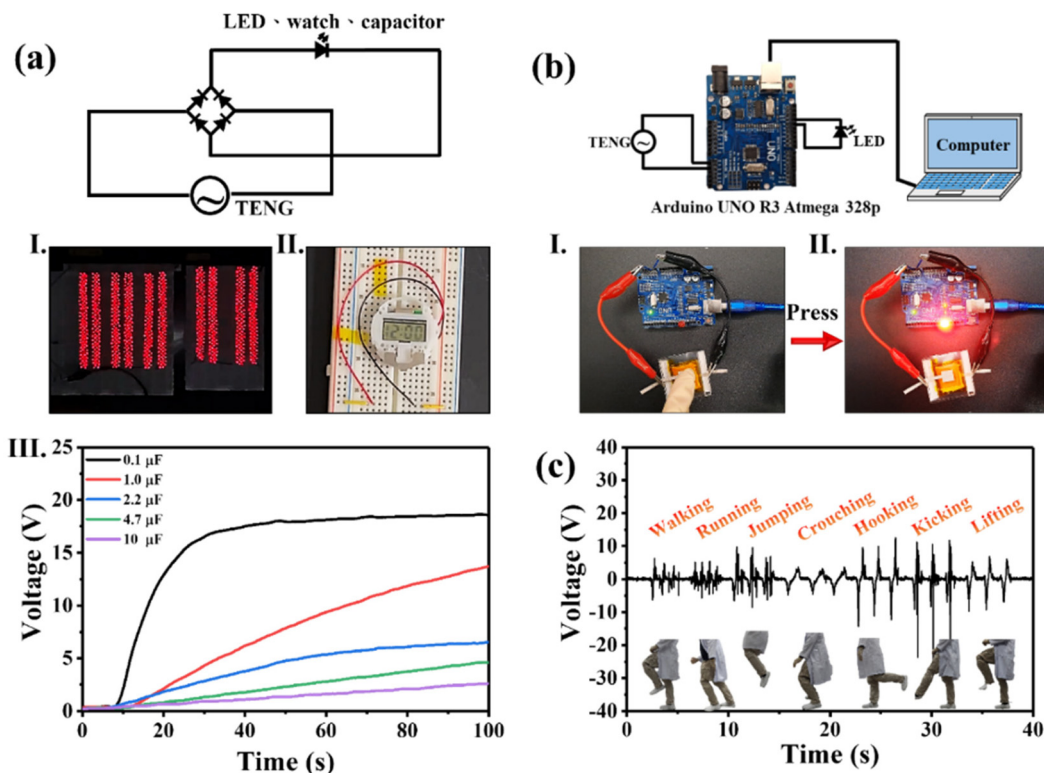

Fig. 5 (a) Schematic representation of the operating circuit for a TENG with a full-wave bridge rectifier for (I) 1000 LED bulbs, (II) a digital watch, and (III) charged capacitors of various capacitances powered using 10 wt% Eu_2O_3–$BaTiO_3$/PVDF-HFP electrospun-nanofiber TENGs. (b) Schematic representation of the operating circuit for a TENG with an Arduino circuit for (I and II) an LED bulb dimmer switch operated using the 10 wt% Eu_2O_3–$BaTiO_3$/PVDF-HFP electrospun-nanofiber TENG as a dominant smart sensor. (c) Output voltages of the 10 wt% Eu_2O_3–$BaTiO_3$/PVDF-HFP electrospun-nanofiber TENG located at the knee of a user performing various leg motions (walking, running, jumping, crouching, hooking, kicking, and lifting).

(Fig. S11†). Notably, the 10 wt% Eu_2O_3–$BaTiO_3$/PVDF-HFP electrospun-nanofiber TENGs could be used not only as self-powering devices but also as sensors. Fig. 5(b) and Movie S2† show the demonstrations of the application of the 10 wt% Eu_2O_3–$BaTiO_3$/PVDF-HFP electrospun-nanofiber TENG as an LED light dimmer switch. When a finger pressed the 10 wt% Eu_2O_3–$BaTiO_3$/PVDF-HFP electrospun-nanofiber TENG, the LED bulb turned on; when pressing the device again, the LED bulb turned off. Furthermore, with continuous pressing of the finger, the light from the LED bulb blinked. In addition, we attached the 10 wt% Eu_2O_3–$BaTiO_3$/PVDF-HFP electrospun-nanofiber TENG at a human knee for use as a sensor to detect leg movement (Movie S3†). During the different phases of leg movement, the 10 wt% Eu_2O_3–$BaTiO_3$/PVDF-HFP electrospun-nanofiber TENG generated different output signals. Therefore, the device could be used, for example, to monitor a patient's recovery by tracking leg movement. These results suggest that our fabricated 10 wt% Eu_2O_3–$BaTiO_3$/PVDF-HFP electrospun-nanofiber TENGs could be used in a wide range of applications, including self-powered devices, e-skins, soft robotics, and healthcare technologies.

Conclusions

We have obtained the highest ever performance from a ceramic powder-based TENG, prepared by incorporating a high-dielectric-constant Eu_2O_3-doped $BaTiO_3$ nanofiller into PVDF-HPF through electrospinning to form the nanofiber mat. The maximum output voltage of our 10 wt% Eu_2O_3–$BaTiO_3$/PVDF-HFP electrospun-nanofiber TENG reached as high as 1004 V with a corresponding current density of 9.9 µA cm^{-2}. The electrical output performance of this system arose from its high dielectric constant and high amounts of transferred charge, allowing it to capture and store triboelectric electrons. The 10 wt% Eu_2O_3–$BaTiO_3$/PVDF-HFP electrospun-nanofiber TENG exhibited a maximum output power density of 12 W m^{-2} at 100 MΩ. This TENG functioned well at various temperatures and humidity points and over longer periods of operation. Furthermore, the developed TENG was stable after 2 weeks, without any degradation. Finally, we applied the developed TENG as an LED light dimmer switch and as a sensor for tracking leg movement. We believe that such TENGs have potential application in self-powered devices, sensors, e-skins, soft robotics, and healthcare technologies.

Author contributions

Xin-Xian Wu organized and integrated the acquired data and wrote the original draft and documents for reviewing. Jun-Jie Zhang conducted the formal analysis and circuit design. Chia-Hsien Lee found the methodology for conducting the experiments. Meng-Fang Lin conceptualized the research idea and supervised the validation of the research and writing for review and editing.

Conflicts of interest

There are no conflicts to declare.

Acknowledgements

References

1 S. A. Han, J. Lee, J. Lin, S.-W. Kim and J. H. Kim, *Nano Energy*, 2019, **57**, 680–691.
2 G. Jian, Q. Meng, Y. Jiao, F. Meng, Y. Cao and M. Wu, *Nanoscale*, 2020, **12**, 14160–14170.
3 M.-F. Lin, K.-W. Chang, C.-H. Lee, X.-X. Wu and Y.-C. Huang, *Sci. Rep.*, 2022, **12**, 14842.
4 J. Xiong, P. Cui, X. Chen, J. Wang, K. Parida, M.-F. Lin and P. S. Lee, *Nat. Commun.*, 2018, **9**, 4280.
5 J. Chen and Z. L. Wang, *Joule*, 2017, **1**, 480–521.
6 Z. L. Wang, *Faraday Discuss.*, 2014, **176**, 447–458.
7 P. Cheng, Y. Liu, Z. Wen, H. Shao, A. Wei, X. Xie, C. Chen, Y. Yang, M. Peng, Q. Zhuo and X. Sun, *Nano Energy*, 2018, **54**, 156–162.
8 J. Kim, H. Ryu, J. H. Lee, U. Khan, S. S. Kwak, H.-J. Yoon and S.-W. Kim, *Adv. Energy Mater.*, 2020, **10**, 1903524.
9 C. Rodrigues, D. Nunes, D. Clemente, N. Mathias, J. M. Correia, P. Rosa-Santos, F. Taveira-Pinto, T. Morais, A. Pereira and J. Ventura, *Energy Environ. Sci.*, 2020, **13**, 2657–2683.
10 Q. Zheng, B. Shi, Z. Li and Z. L. Wang, *Adv. Sci.*, 2017, **4**, 1700029.
11 Y. J. Kim, J. Lee, S. Park, C. Park, C. Park and H.-J. Choi, *RSC Adv.*, 2017, **7**, 49368–49373.
12 X. J. Zhao, G. Zhu and Z. L. Wang, *ACS Appl. Mater. Interfaces*, 2015, **7**, 6025–6029.
13 J. M. Wu, C. K. Chang and Y. T. Chang, *Nano Energy*, 2016, **19**, 39–47.
14 S. Wang, Y. Zi, Y. S. Zhou, S. Li, F. Fan, L. Lin and Z. L. Wang, *J. Mater. Chem. A*, 2016, **4**, 3728–3734.
15 K.-E. Byun, Y. Cho, M. Seol, S. Kim, S.-W. Kim, H.-J. Shin, S. Park and S. Hwang, *ACS Appl. Mater. Interfaces*, 2016, **8**, 18519–18525.
16 C. Wu, T. W. Kim and H. Y. Choi, *Nano Energy*, 2017, **32**, 542–550.
17 G. Song, Y. Kim, S. Yu, M.-O. Kim, S.-H. Park, S. M. Cho, D. B. Velusamy, S. H. Cho, K. L. Kim, J. Kim, E. Kim and C. Park, *Chem. Mater.*, 2015, **27**, 4749–4755.
18 F.-R. Fan, L. Lin, G. Zhu, W. Wu, R. Zhang and Z. L. Wang, *Nano Lett.*, 2012, **12**, 3109–3114.

19 C. K. Jeong, K. M. Baek, S. Niu, T. W. Nam, Y. H. Hur, D. Y. Park, G.-T. Hwang, M. Byun, Z. L. Wang, Y. S. Jung and K. J. Lee, *Nano Lett.*, 2014, **14**, 7031–7038.

20 Z.-H. Lin, Y. Xie, Y. Yang, S. Wang, G. Zhu and Z. L. Wang, *ACS Nano*, 2013, **7**, 4554–4560.

21 S. Wang, L. Lin and Z. L. Wang, *Nano Lett.*, 2012, **12**, 6339–6346.

22 Z. L. Wang, *Nano Energy*, 2020, **68**, 104272.

23 X.-S. Zhang, M.-D. Han, R.-X. Wang, F.-Y. Zhu, Z.-H. Li, W. Wang and H.-X. Zhang, *Nano Lett.*, 2013, **13**, 1168–1172.

24 D. Kim, S.-B. Jeon, J. Y. Kim, M.-L. Seol, S. O. Kim and Y.-K. Choi, *Nano Energy*, 2015, **12**, 331–338.

25 D. Kim, I.-W. Tcho, I. K. Jin, S.-J. Park, S.-B. Jeon, W.-G. Kim, H.-S. Cho, H.-S. Lee, S. C. Jeoung and Y.-K. Choi, *Nano Energy*, 2017, **35**, 379–386.

26 J. Huang, X. Fu, G. Liu, S. Xu, X. Li, C. Zhang and L. Jiang, *Nano Energy*, 2019, **62**, 638–644.

27 N. Zhang, F. Huang, S. Zhao, X. Lv, Y. Zhou, S. Xiang, S. Xu, Y. Li, G. Chen, C. Tao, Y. Nie, J. Chen and X. Fan, *Matter*, 2020, **2**, 1260–1269.

28 J. Xiong, M. Almeida and C. A. O'Brien, *Bone*, 2018, **112**, 1–9.

29 J. Zhao, W. Zhu, X. Wang, L. Liu, J. Yu and B. Ding, *ACS Nano*, 2020, **14**, 1045–1054.

30 V. Sencadas, C. Garvey, S. Mudie, J. J. K. Kirkensgaard, G. Gouadec and S. Hauser, *Nano Energy*, 2019, **66**, 104106.

31 X. Wang, Y. Zhang, X. Zhang, Z. Huo, X. Li, M. Que, Z. Peng, H. Wang and C. Pan, *Adv. Mater.*, 2018, **30**, 1706738.

32 A. R. Mule, B. Dudem, H. Patnam, S. A. Graham and J. S. Yu, *ACS Sustainable Chem. Eng.*, 2019, **7**, 16450–16458.

33 Y. Liu, L. Wang, L. Zhao, K. Yao, Z. Xie, Y. Zi and X. Yu, *Adv. Electron. Mater.*, 2020, **6**, 1901174.

34 J. Yu, X. Hou, J. He, M. Cui, C. Wang, W. Geng, J. Mu, B. Han and X. Chou, *Nano Energy*, 2020, **69**, 104437.

35 Y. Li, J. Xiong, J. Lv, J. Chen, D. Gao, X. Zhang and P. S. Lee, *Nano Energy*, 2020, **78**, 105358.

36 X. Pu, J.-W. Zha, C.-L. Zhao, S.-B. Gong, J.-F. Gao and R. K. Y. Li, *Chem. Eng. J.*, 2020, **398**, 125526.

37 J. W. Lee, H. J. Cho, J. Chun, K. N. Kim, S. Kim, C. W. Ahn, I. W. Kim, J.-Y. Kim, S.-W. Kim, C. Yang and J. M. Baik, *Sci. Adv.*, 2017, **3**, e1602902.

38 T. Bhatta, P. Maharjan, H. Cho, C. Park, S. H. Yoon, S. Sharma, M. Salauddin, M. T. Rahman, S. M. S. Rana and J. Y. Park, *Nano Energy*, 2021, **81**, 105670.

39 H. H. Singh and N. Khare, *Energy*, 2019, **178**, 765–771.

40 J. Chen, H. Guo, X. He, G. Liu, Y. Xi, H. Shi and C. Hu, *ACS Appl. Mater. Interfaces*, 2016, **8**, 736–744.

41 S. Paria, S. K. Si, S. K. Karan, A. K. Das, A. Maitra, R. Bera, L. Halder, A. Bera, A. De and B. B. Khatua, *J. Mater. Chem. A*, 2019, **7**, 3979–3991.

42 X. Kang, C. Pan, Y. Chen and X. Pu, *RSC Adv.*, 2020, **10**, 17752–17759.

43 X. Tao, H. Jin, M. Ma, L. Quan, J. Chen, S. Dong, H. Zhang, C. Lv, Y. Fu and J. Luo, *Phys. Status Solidi A*, 2019, **216**, 1900068.

44 G. Min, A. Pullanchiyodan, A. S. Dahiya, E. S. Hosseini, Y. Xu, D. M. Mulvihill and R. Dahiya, *Nano Energy*, 2021, **90**, 106600.

45 P. Zhang, W. Zhang, L. Deng and H. Zhang, *Nano Energy*, 2021, **87**, 106176.

46 Z. Fang, K. H. Chan, X. Lu, C. F. Tan and G. W. Ho, *J. Mater. Chem. A*, 2018, **6**, 52–57.

47 L. Shi, H. Jin, S. Dong, S. Huang, H. Kuang, H. Xu, J. Chen, W. Xuan, S. Zhang, S. Li, X. Wang and J. Luo, *Nano Energy*, 2021, **80**, 105599.

48 M.-F. Lin, V. K. Thakur, E. J. Tan and P. S. Lee, *J. Mater. Chem.*, 2011, **21**, 16500–16504.

49 G. J. Choi, S. K. Lee, K. J. Woo, K. K. Koo and Y. S. Cho, *Chem. Mater.*, 1998, **10**, 4104–4113.

50 D. F. K. Hennings, C. Metzmacher and B. S. Schreinemacher, *J. Am. Ceram. Soc.*, 2001, **84**, 179–182.

51 J. O. Eckert Jr., C. C. Hung-Houston, B. L. Gersten, M. M. Lencka and R. E. Riman, *J. Am. Ceram. Soc.*, 1996, **79**, 2929–2939.

52 M. L. Moreira, G. P. Mambrini, D. P. Volanti, E. R. Leite, M. O. Orlandi, P. S. Pizani, V. R. Mastelaro, C. O. Paiva-Santos, E. Longo and J. A. Varela, *Chem. Mater.*, 2008, **20**, 5381–5387.

53 L. H. Robins, D. L. Kaiser, L. D. Rotter, P. K. Schenck, G. T. Stauf and D. Rytz, *J. Appl. Phys.*, 1994, **76**, 7487–7498.

54 J.-H. Zhang, Y. Li, J. Du, X. Hao and H. Huang, *J. Mater. Chem. A*, 2019, **7**, 11724–11733.

55 W. Ma, J. Zhang, S. Chen and X. Wang, *Appl. Surf. Sci.*, 2008, **254**, 5635–5642.

56 D. Hou, D. Lin, C. Ding, D. Wang and J. Wang, *Sep. Purif. Technol.*, 2017, **189**, 82–89.

57 G. Chen, X. Wang, J. Lin, W. Yang, H. Li, Y. Wen, L. Li, Z. Jiang and Q. Lei, *J. Mater. Chem. C*, 2016, **4**, 8070–8076.

58 H. Liu, Y. Feng, J. Shao, Y. Chen, Z. L. Wang, H. Li, X. Chen and Z. Bian, *Nano Energy*, 2020, **70**, 104499.

59 J.-H. Zhang, Z. Zhou, J. Li, B. Shen, T. Zhu, X. Gao, R. Tao, X. Guo, X. Hu, Y. Shi and L. Pan, *ACS Mater. Lett.*, 2022, **4**, 847–852.

60 K. Zhao, J. Meng, M. Zhong, S. Li, Y. Niu, H. Liu, B.-N. Gu, M.-J. Liu, D. Zhang, L. Kong and Y.-L. Chueh, *Small*, 2022, **18**, 2202792.